

An Experimental Study of Plasma Detachment from a Magnetic Nozzle in the Plume of the VASIMR[®] Engine

IEPC-2013-123

*Presented at the 33rd International Electric Propulsion Conference,
The George Washington University • Washington, D.C. • USA
October 6 – 10, 2013*

Christopher S. Olsen¹, Maxwell G. Ballenger², Mark D. Carter³, Franklin R. Chang Díaz⁴, Matthew Giambusso⁵,
Timothy W. Glover⁶, Andrew V. Ilin⁷, and Jared P. Squire⁸
Ad Astra Rocket Company, Webster, Texas, 77598, USA

Benjamin W. Longmier⁹
University of Michigan, Department of Aerospace Engineering, Ann Arbor, Michigan, 48109, USA

Edgar A. Bering, III¹⁰
University of Houston, Department of Physics and ECE, Houston, Texas, 77204, USA

and

Paul A. Cloutier¹¹
Rice University, Department of Physics and Astronomy, Houston, Texas, 77005, USA

Abstract: Understanding the physics involved in plasma detachment from magnetic nozzles is well theorized but lacking in large scale experimental support. We have undertaken an experiment using the 150 m³ VASIMR[®] test facility and VX-200 thruster seeking evidence that detachment occurs and understanding of the physical processes involved. It was found that the plasma jet in this experiment does indeed detach from the applied magnetic nozzle (peak field ~ 2 T) in a two part process. The first part involves the ions beginning to deviate from the nozzle field 0.8 m downstream of the nozzle throat. This separation location is consistent with a loss of adiabaticity where the ratio of the ion Larmor radius to the magnetic field scale length ($r_{Li} |\nabla B|/B$) becomes of order unity and conservation of the magnetic moment breaks down. Downstream of this separation region the dynamics of the unmagnetized ions and magnetized electrons, along with the ion momentum, affect the plume trajectory. The second part of the process involves the formation of plasma turbulence in the form of high frequency electric fields. The ion and electron responses to these electric fields depend upon ion momentum, magnetic field line curvature, magnetic field strength, angle between the particle trajectories, and the effective momentum transfer

¹ Senior Research Scientist, chris.olsen@adastrarocket.com.

² Staff Scientist, ballenger@gmail.com.

³ Director of Technology, mark.carter@adastrarocket.com

⁴ Chief Executive Officer, info@adastrarocket.com

⁵ Research Scientist, matthew.giambusso@adastrarocket.com

⁶ Director of Development, tim.glover@adastrarocket.com

⁷ Computational Research Lead, andrew.ilin@adastrarocket.com

⁸ Director of Research, jared.squire@adastrarocket.com

⁹ Assistant Professor, longmier@umich.edu

¹⁰ Professor, eabering@uh.edu

¹¹ Professor Emeritus, pac@rice.edu

time. In stronger magnetic field regions of the nozzle, the detached ion trajectories are affected such that the unmagnetized ions begin to flare radially outward. Further downstream as the magnetic field weakens, for higher ion momentum and along the edge of the plume, the fluctuating electric field enables anomalous cross-field electron transport to become more dominant. This cross-field transport occurs until the electric fields dissipate approximately 2 m downstream of the nozzle throat and the ion trajectories become ballistic. This transition to ballistic flow correlates well with the sub-to-super Alfvénic flow transition (β_k). There was no significant change observed to the applied magnetic field.

Nomenclature

ICH	= ion cyclotron heating	R_c	= radius of curvature [m]
$\Omega_{c,e,i}$	= generic, electron, ion cyclotron frequency	Γ_{iz}	= axial ion flux [ions/s]
$\beta_{k,th}$	= kinetic, thermal beta	Φ_B	= axial magnetic flux [Wb]
B	= magnetic flux density [G]	J_{iz}	= axial current density [A/m ²]
D	= diffusion coefficient [m ² /s]	f_i	= ion flux plume fraction
μ	= mobility [m ² /V/s]	f_ϕ	= magnetic flux plume fraction
ν	= collision frequency [Hz]	r_{Li}	= Larmor radius [m]
S, L	= external ionization sources/losses [ions/s/m ²]	E	= electric field [V/m]
u, v_i	= ion velocity [m/s]	q	= elementary charge [C]
η	= plasma resistivity [ohm]	E_i	= ion energy [eV]
u_{de}	= drift velocity of electrons relative to ions [m/s]	ρ	= mass density [kg/m ³]
τ_{eff}	= effective momentum transfer time [s]	f_{LH}	= lower hybrid frequency [Hz]
r_{edge}	= projected magnetic plasma boundary [m]	$m_{e,i}$	= electron, ion mass [kg]
V	= test particle velocity [m/s]	n_e	= electron density [m ⁻³]
u_\perp	= cross-field electron velocity [m/s]	T_e	= electron temperature [eV]
u_E	= $E \times B$ drift velocity [m/s]	k_B	= Boltzmann constant [erg/eV]
u_D	= diamagnetic drift velocity [m/s]	ϵ_0	= permittivity of free space [F/C]
$\phi(x)$	= error function	$\ln A$	= Coulomb logarithm
$\psi(x)$	= first derivative of error function	θ	= pitch, divergence angle [°]

I. Introduction

Plasma flowing through magnetic nozzles has been observed in many natural systems and is used in a variety of terrestrial applications ranging from plasma processing to electric propulsion^{1,2}. Similar to de Laval nozzles that convert random thermal motion into directed flow, magnetic nozzles are used to redirect the motion and momentum of the plasma flowing through the nozzle. To this end, a magnetic nozzle can be used to improve thrust efficiency and provide a means of controlling the plume geometry and plasma energy distribution functions. One issue facing the implementation of magnetic nozzles is the tendency of the plasma to remain magnetized or otherwise tied to the magnetic field lines forming the nozzle. Many theories have been proposed to address the physics of the plasma detachment process from magnetic nozzles that range from collisional resistive diffusion³ to collisionless magnetohydrodynamic field line stretching^{4,5}, loss of adiabaticity^{6,7}, and electron inertia^{8,9}. Despite the many theories attempting to explain this process, there has been an overall dearth of quality experimental data to fully support any one mechanism, and as a result knowledge of the physics of magnetic nozzles remains limited.

One device that is ideally suited to study the processes involved in magnetic nozzle plasma detachment is the VASIMR[®] VX-200 laboratory device¹⁰. A dipole-expanding magnetic nozzle is inherent to the design and the ion cyclotron resonance process in the second stage of the plasma rocket allows control of the ion energy, thus permitting the investigation into momentum-dependent detachment processes. Other main benefits of using this device are that it is situated within a 150 m³ vacuum facility where the plume is able to expand for several meters before terminating on any material surface, the pumping rate is sufficient to keep background neutral pressures low enough to minimize charge-exchange processes, and ramp to full power plasma operation within 100 ms is routine. An extensive experiment campaign where detailed mapping of the plasma plume in a volume extending more than 2 m downstream of the exhaust exit has been completed using the VASIMR[®] VX-200 device operating at two power levels; 30±0.4 kW and 100±2 kW corresponding to the first stage helicon discharge alone and both stages together, respectively². Data were taken during the early portions of the discharge while background pressure remained below

2×10^{-4} torr. A variety of traditional plasma diagnostics were used to gather plume data. The plume mapping was performed by repositioning each of the diagnostics using a 2-axis step-motor driven translation stage with sub-millimeter resolution. The spatially dependent plume data were then analyzed to verify if separation of the plasma from the applied magnetic field had occurred and which of the leading detachment theories were most consistent with the data. This paper shall attempt to summarize the highlights of this experiment and provide new key insights into the physics of energized plasma flowing through an axial magnetic nozzle.

The organization of the rest of this paper shall be as follows: Section II shall describe the key components of the experiment such as the plasma source, environmental conditions, and plasma diagnostics showing that the setup is legitimate and the data taken is of high quality. Section III will discuss the results of the data characterizing the behavior of the plume flowing in the conditions listed in section II. Section IV will close the paper with some of the general outcomes of the work while proposing some future experiments and applications of magnetic nozzles.

II. Experimental Setup

A laboratory experiment set on adequately measuring and quantifying the physics involved in the final stages of plasma flowing through a magnetic nozzle, the separation of the magnetized plasma from the field lines that form the nozzle, should have to meet a number of specific required conditions^{1,11}. The first of which is that the system be large enough for the detachment process to occur and that it have ample volume for the plume to expand unimpeded prior to neutralizing on the walls of the chamber. The second requirement is to have sufficiently low vacuum conditions so as to minimize plasma to neutral interactions (e.g. particle sources and losses due to impact ionization or charge-exchange interactions) which will alter unimpeded fluxes and potentially mask the underlying physics. A third requirement involves exploring over an adequate scale length for a magnetic nozzle where the magnetic field strengths extend a few orders of magnitude so as to test over a wide range of potential physical processes. Lastly, the experiment should be capable of measuring the relevant plasma properties across the scale length of the system enough to characterize the detachment process. The following sub-sections will address that each of these requirements were met during our experiment. We begin with an overview of the plasma source and magnetic nozzle followed by descriptions of the vacuum facility used to create the proper conditions and plasma diagnostics needed to measure the plasma.

A. VASIMR® VX-200 Engine

The Variable Specific Impulse Magnetoplasma Rocket (VASIMR®) engine is a high power electric propulsion system capable of varying the thrust and specific impulse while operating at a fixed input power. This form of constant power throttling makes the VASIMR® engine an attractive option for a wide range of prospective space missions. The main components of a VASIMR® engine are the engine core, propellant source, magnet, and RF generators and are displayed in Fig. 1. A key benefit in using the VASIMR® engine to study magnetic nozzles is the magnetic field inherent to the design. The properly shaped field profile enables radio frequency (RF) wave transport and forms a dipole (far field) expanding nozzle. Plasma is generated by a 6.78 MHz high power helicon¹¹⁻¹⁷ which serves as the first stage of the engine core. The second stage (known as ion cyclotron heating or ICH) energizes the ions by launching left-hand polarized slow mode waves from the high field side of ion resonance.¹⁸⁻²⁰ This RF wave coupling mechanism requires that the plasma be fully magnetized and enables control of the ion velocity exiting the thruster.

The VX-200 (VASIMR® experimental - 200 kW) device is a laboratory prototype operating from 2009 – 2012 demonstrating high power densities (6 MW/m^2 across the exit area), specific impulse ranging between 2000 s to 5000 s, and thrust up to 6 N. The magnetic field is generated by a cryogen-free,

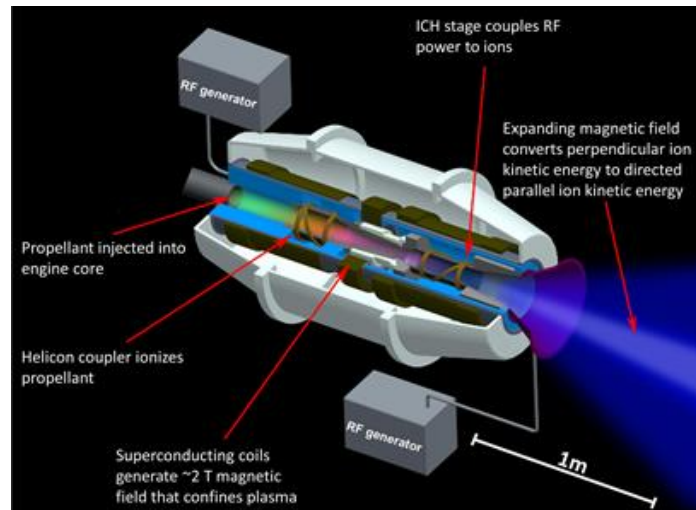


Figure 1. Conceptual schematic of the VASIMR® engine.

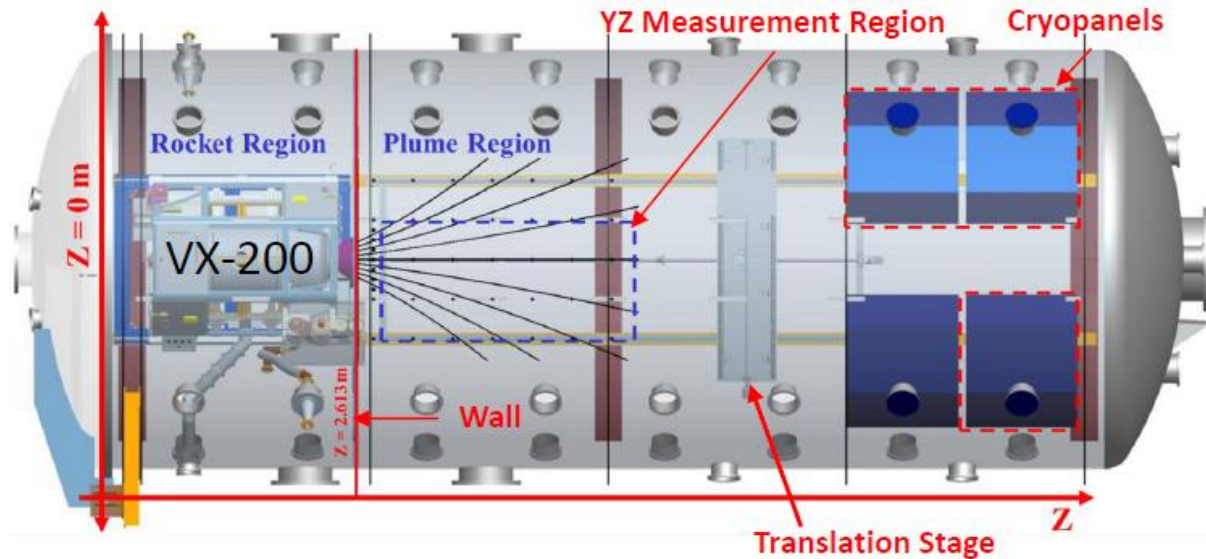


Figure 2. Semi-transparent schematic of the 10 m long x 4.3 m diameter vacuum chamber and the VX-200 engine. Also shown are the translation stage, cryopumps, and locations of the measurement region and vacuum partition. All axial coordinates reference the end flange of the chamber.

first generation (Nb-Ti) superconducting magnet encased in a well-insulated cryostat surrounding the engine core. It features a lightweight design and was fabricated by Scientific Magnetics of Oxford England, and produces a peak magnetic field strength of 2 T. The RF power is generated from two high-efficiency solid-state generators (combined conversion efficiency of 95% DC to RF) manufactured by Nautel Limited of Canada, and are independently controlled²¹. Impedance matching circuits are used to couple up to 98% of the RF power into the plasma. The RF generators are controlled using an in-house developed FPGA circuit that provides precise synchronization between the units. Argon propellant is regulated through an injector plate into the first stage using a Moog propellant manifold. The manifold contains a proportional flow control valve (PFCV), Taber Industries low pressure transducer, and a 0.041" diameter orifice flow controller. Choked flow enables mass flow rates up to 5000 sccm (~ 150 mg/s) which are verified using an in-line calibrated, NIST traceable, MKS-179 thermal mass flow controller. While the magnetic field is consistently active, timing of the gas flow, RF Power, and plasma diagnostics are performed using a fiber optic triggering system synchronizing each system to within 6 ms from receiving the command.

B. Vacuum Facility

The experiment was carried out in a stainless steel vacuum chamber that is 4.3 m in diameter and 10 m long with a volume of 150 m³ (including the end caps) located at the Ad Astra Rocket Company's Houston facility (Fig. 2). One end opens fully for complete access to the inner diameter of the chamber. The chamber is partitioned into two regions: a rocket region and a plume region. An anodized aluminum framed wall with Lexan paneling serves as the partition which is located at 2.613 m (nozzle 'throat' is at ~ 2.08 m) with Z = 0 m defined at the chamber door flange. The VX-200 engine is installed in the forward section of the chamber where a separate cryopump is used to maintain a lower pressure during firings so as to prevent arcing and glow discharges from forming near high voltage RF components. The majority of the VX-200 components are located within the vacuum chamber with only the RF generators, magnet power supplies, and magnet cryocoolers maintained at atmospheric pressure. The plume region contains four CVI Torr-Master 1200i cryopumps, although for this experiment only three were used for a cumulative argon pumping speed of 175,000 l/s and an ultimate pressure of ~ 1x10⁻⁸ torr. The

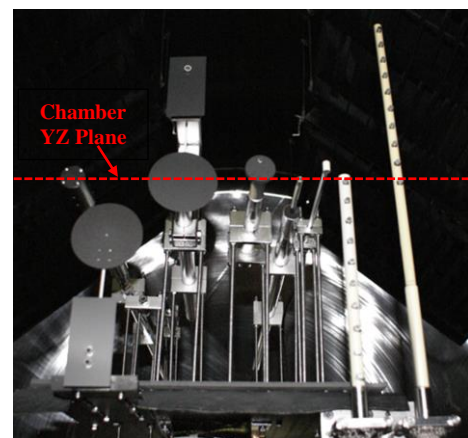


Figure 3. Image of plasma diagnostics mounted on the translation stage.

normal baseline pressure in between firings is $\sim 5 \times 10^{-8}$ torr and rises as high as 2×10^{-4} torr argon after 1 s of plasma operation. Pressures in the plume region are measured using three separate hot cathode ion gauges.

C. Diagnostics and Translation Stage

In order to adequately measure many of the plasma properties relevant for characterizing the physics of plasma detachment from magnetic nozzles (e.g. plasma density, magnetic field strength, ion velocity, etc.), a wide variety of plasma diagnostics should be used over the spatial range where detachment may be occurring. The diagnostic used in this study are shown in Fig. 3. They are (from left to right): Retarding Potential Analyzer (RPA), HF electric field probe (recessed), backup plasma momentum flux sensor (PMFS), primary PMFS, 3-axis magnetometer, guard-ring Langmuir probe, azimuthal flux probe, lower ion flux probe array, and upper ion flux probe array. Most of these plasma probes are situated with its primary sensor or collector along the horizontal YZ plane of the rocket/chamber. Descriptions of each of the diagnostics pertinent to this study, including translation stage are detailed below.

1. Langmuir Probes

There were two separate implementations of ‘single’ planar Langmuir probes mounted on the translation stage: A variable bias guard-ring probe²², and fixed bias ion flux probes. A single collector guard-ring probe was used to collect full I-V characteristics of the plasma whose bias ranged from -46 VDC to +48 VDC. This particular probe was not RF compensated, but it has been characterized²³ under similar RF conditions to this experiment and the uncertainty is propagated through the data. The collector is surrounded by a stainless steel guard-ring at a gap distance of 0.13 mm to minimize sheath expansion effects. A pair of ten-collector fixed bias Langmuir probe arrays, spaced orthogonally along an alumina tube (Fig. 3), were used to measure ion flux. These ion flux probes were biased at -20 VDC into the ion saturation regime which was verified to be $3T_e$ more negative than the floating potential during each firing using the guard-ring I-V characteristics. The collectors for all of the Langmuir probes consisted of high purity 0.64 cm diameter molybdenum machined into a terraced design²⁴.

2. Plasma Momentum Flux Sensor

A plasma momentum flux sensor (PMFS) was used to measure the amount of force imparted to the thruster carried away within the plasma stream. This method of measuring force has been characterized elsewhere²⁵⁻²⁷ and is an inexpensive alternative to traditional inverted pendulum thrust stands comparing well using the P5 Hall thruster.²⁸ The PMFS consists of a 9 cm diameter pyrolytic graphite disc attached to a 0.1 cm x 0.1 cm x 10 cm insulating alumina rod. The opposite end of this stiff shaft is mechanically attached to a 5.7 cm x 1.3 cm titanium bar where 4 Czochralski pulled boron doped silicon strain gauges are fixed to the titanium and connected in a Wheatstone bridge configuration. The output voltage is directly proportional to the amount of force causing strain. A small graphite shield is used to shadow the titanium bar/strain gauge assembly from the flowing plasma. The sensor is calibrated using tension applied from a set of precision masses and has a resolution of 0.1 mN. The probe has a natural frequency of oscillations of ~ 40 Hz and at least 3-4 periods (~ 100 ms) were averaged at minimum during data analysis.

3. Retarding Potential Analyzer

A retarding potential analyzer (RPA) was used to deduce information about the ion distribution function (e.g. the parallel ion energy and temperature). This instrument was designed and maintained by the University of Houston and featured a 4 double grid arrangement.¹⁹ The grids consisted of 35.4 wires/cm nickel mesh and spaced 0.1 cm apart using alumina spacers. Plasma passes through a 1 cm diameter graphite aperture before encountering an attenuation grid, a primary electron suppressor, an ion discriminator or sweep grid, and secondary electron suppressor prior to terminating on a molybdenum collector. The attenuation grid reduces the plasma density to permit the primary electron suppressor to repel incoming electrons. A variable bias voltage on the ion discriminator repels ions with flow kinetic energies below this retarding electrostatic potential while those above will reach the collector. A secondary electron suppressor removes downstream electrons formed from secondary effects (i.e. secondary electron emission). The ion exhaust velocity and temperature are deduced from the current-retarding potential data using least-squares fits of drifting Maxwellians which are a common analytical method for spacecraft RPA data.^{29,30} This RPA was mounted at the end of a step-motor driven goniometer which permitted up to 90° articulation of the RPA head and analysis of parallel to perpendicular ion pitch angles. It has been estimated that this RPA is able to resolve multiple component ion populations as well as multiply ionized species, appearing as a stepped current-voltage characteristic, and are analyzed by fitting a multi-component distribution.^{16,31}

4. Magnetometer

Magnetic field measurements were made using an F. W. Bell 7030 Gauss/Tesla Meter using a ZOF73-3208-30-T 3-axis Hall probe. The Hall sensor elements are arranged orthogonally at the end of a 20.3 cm long aluminum fixture. Each Hall sensor has a capable range of 0 to 30 kG, a resolution of 0.1 mG, and is accurate to within 2%. The sensors are temperature compensated correcting to approximately $-0.05\%/^{\circ}\text{C}$ of temperature change. The Hall probe itself was thermally protected from the plasma flow as it was mounted within a round capped alumina sleeve in addition to being shadowed by a 3.8 cm diameter graphite disk (Fig. 3). This instrument may be used to measure magnetic fields from DC up to 50 kHz. A malfunction on one of the axis during an earlier detachment experiment made it necessary to have the instrument recalibrated. The 3-axis probe, full cable assemblies, and electronics box were calibrated to the ISO/EIC 17025 standard which is the most rigorous and legally traceable calibration standard offered for this instrument. The experiment was repeated at a slightly lower mass flow rate.

5. High Frequency Electric Field Probe

Having adequate information on the electric field, particularly the oscillating electric field, is important when studying charged particle flows. Knowledge of the range of frequencies and magnitude of electric fields in the plasma is telling to particle transport and instabilities that may exist throughout the magnetic nozzle system. The probe used to measure the oscillating electric field was designed and fabricated by the Alfvén lab in Stockholm and have used this type of probe previously to measure high frequency electric characteristics in a plasma gun.^{32,33} It consists of a pair of 5 mm long by 0.3 mm diameter tungsten electrodes separated by 11.9 mm, along the Y axis, which are inserted into the plasma stream. Wire leads to the electrodes pass through alumina capillary tubing and multi-bore alumina tubing and terminate on a common transistor socket. The capillary tubing and alumina shaft are bonded using Torr-Seal, a thermally limited sealant, which prevented us from fully extending the axial range of this probe into the high heat flux during ICH plasma. The probe was therefore recessed 33 cm behind the leading plane of the other diagnostics (Fig. 3). None-the-less the probe was adequately exposed to the plasma stream.

The leads of the electrodes were passed through a SRS SIM910 JFET voltage preamp and fed into an Agilent 4395A Network/Spectrum/Vector analyzer which measured the power spectrum between the electrodes. Spectra were taken every 500 ms from 0 to 10 MHz in steps of 12.5 kHz. The frequency dependent electric field is found using the peak-peak voltage backed out of the power spectrum divided by the separation distance of the electrodes. To reduce uncertainty ensemble smoothing was used to average several spectra taken during the same firing.³⁴ The probe, cabling, and electronics were in situ calibrated end to end over a 10 MHz frequency range by applying a 1 V_{pp} sinusoid across the electrodes using an Agilent 33220A waveform generator.¹ The corresponding gain function was used to produce electric field spectra. Considering the probe operates in an RF environment, a vacuum (out of the plasma) spectrum was subtracted off of the composite voltage spectrum. Mapping out the electric field spectra, as is shown in this paper, is important for understanding cross-field transport of electrons in the magnetic nozzle.

6. Translation Stage

Most of the plasma diagnostics used in this magnetic nozzle study were fixed on top of a movable 2-axis translation stage. Each axis of the 2 m by 5 m translation stage was ball-screw driven using high-torque vacuum rated stepper motors from Lin Engineering. Microstepping features combined with the fine thread pitch of the ball-screws and low backlash results in 0.1 mm position resolution. Positions are calibrated using fixed inductive limit sensors referenced to the vacuum chamber door flange (Fig. 2). The movable portion of the translation stage is an elevated aluminum plate featuring regularly gridded tapped holes similar to an optical bench. The plasma diagnostics are further elevated above this aluminum plate to the chamber/nozzle centerline using threaded stainless steel rods. Exposed aluminum is covered by Grafoil™ sheets and pure graphite plate to minimize sputtering from the plasma stream.

D. Data Acquisition and Shot Parameters

An operational flowchart of a typical VX-200 firing showing synchronization of the gas, RF power, and data acquisition modules is shown in

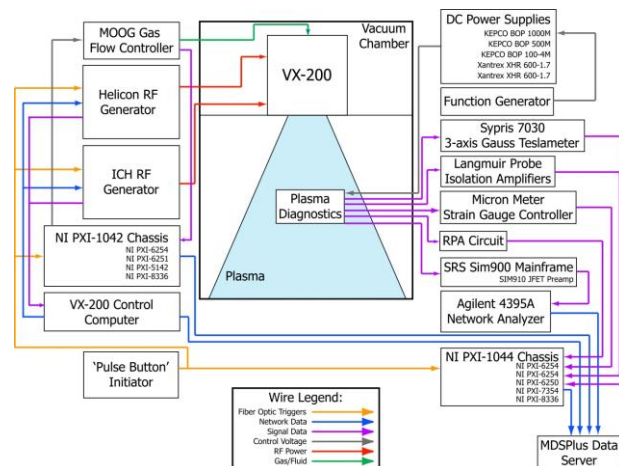


Figure 4. Operational flowchart of a VX-200 firing.

Fig. 4. A user depresses a physical ‘pulse’ button initiating the firing sequence by launching a fiber optic pulse that is converted into a digital waveform and fed into the RF generators and National Instruments PXI chassis. The rising edge of this waveform causes the commanded pre-programmed gas flow and RF power profiles to run while NI multifunction DAQ cards fill up sample buffers at rates of 40 kHz and 100 kHz depending upon the specific diagnostic. For this experiment a 2 s sample buffer is sufficient to collect plume data for a standard 100 kW power shot as shown in Fig. 5. The solid lines are shot-averaged over the entire experiment totaling more than 450 firings. Dashed lines represent 1σ uncertainty bounds to the averages. Despite the VX-200 laboratory device being capable of operating at 200 kW input power for short periods, due to the high rate of repetition it was decided to perform the experiment at reduced power so as not to overstress the device thus increasing the likelihood of finishing the tests without interruption.

For the purposes of data analysis, consistent data windows for each firing were from 0.4 s to 0.5 s for the first stage and 0.65 s to 0.75 s with the addition of the second stage. This corresponded to average power levels of 30 ± 0.4 kW and 100 ± 2 kW, respectively. The mass flow rate remained constant to within 0.5 sccm argon during these time spans. The exhaust region neutral pressure, as measured by separate ion gauges, was kept below 10^{-4} torr during these windows permitting charge-exchange mean free paths greater than 12.6 m and 1.3 m, respectively.

Since the aim of this experiment is to map out plasma properties in the plume, the translation stage was used to reposition the probes in between successive firings. The chosen approach was to perform radial position scans at fixed axial intervals with respect to the closest measurement location (~ 0.7 m downstream the nozzle throat); a radial scan every $\Delta Z = 0.1$ m for the closest 1.0 m, $\Delta Z = 0.2$ m for next 0.4 m, and $\Delta Z = 0.4$ m for the final 0.8 m. The axial magnetic field strength decreases nearly two orders of magnitude over this span ($B_z \sim 740$ G to 10 G). Each radial scan consisted of moving the translation stage from chamber centerline out to $R = 0.9$ m at intervals of $\Delta R = 0.05$ m in addition to allocating a firing to each plasma diagnostic when positioned along the nozzle axis creating higher spatial resolution near the center of the plume.

III. Experimental Results and Discussion

This is the first time a detailed large scale 2D mapping of plume flow through an axial magnetic nozzle has been performed with the aim of studying the physics of plasma separation from the applied magnetic field. In determining plasma detachment, there are two challenges that need to be resolved; 1) gain evidence that detachment has occurred and 2) verify if any currently accepted theories are applicable based on the behavior of the flow. For the first challenge, a simplified view of the problem of actually measuring plasma detachment is to see if the measured flow does not expand at the same rate at the magnetic field. An initial approach to quantify this notion is to compare the expansion of certain plasma parameters along the axis of the nozzle. Ion flux, momentum flux, magnetic flux, and

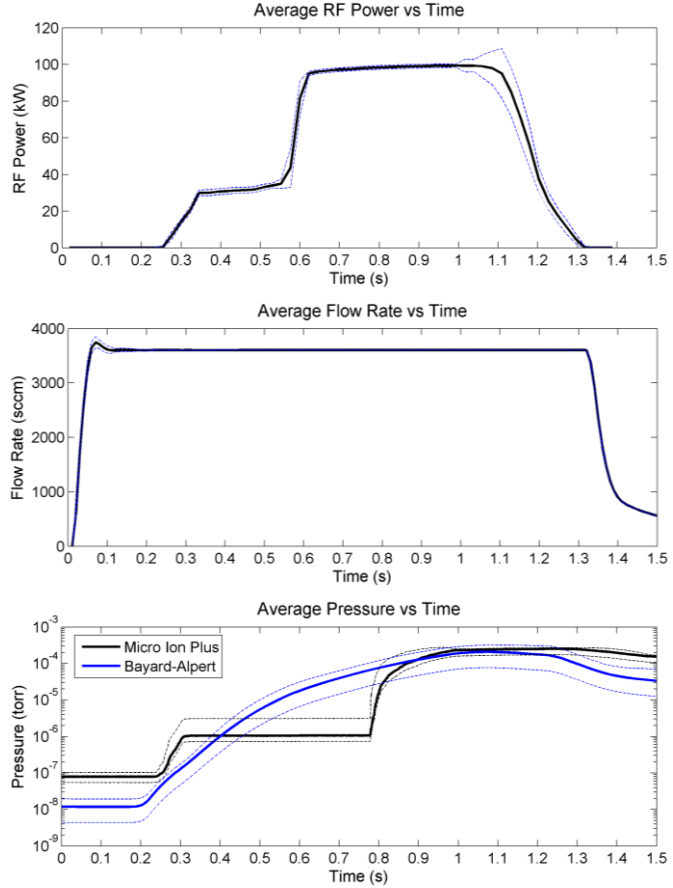


Figure 5. Standard shot configuration including uncertainty bounds (dashed lines). Data analysis windows for the low and high power configurations were taken from 0.4-0.5 s and 0.65-0.75 s respectively. (top) Average RF forward power profile. (middle) Steady 3600 sccm (~ 107 mg/s) argon flow. (bottom) Exhaust region chamber pressure measured by separate hot cathode ion gauges.

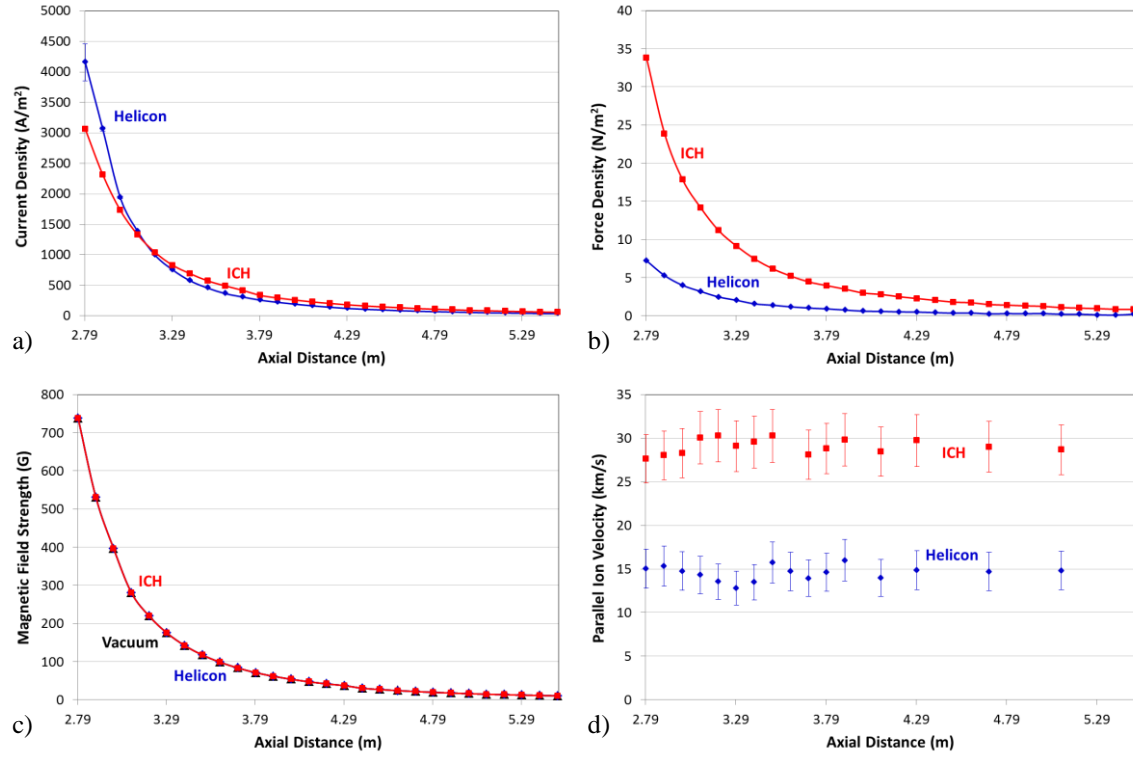


Figure 6. Data taken along nozzle axis for the (a) ion flux, (b) momentum flux, (c) magnetic flux, and (d) parallel ion velocity during both helicon only (blue) and helicon + ICH (red) modes of operation. The applied (vacuum) magnetic field data is also shown (black). Error bars are displayed showing systematic uncertainty and were obtained through repeated firings.

parallel ion velocity data taken along the nozzle axis during both the helicon and helicon + ICH time windows are displayed in Fig. 6.

There are several significant observations regarding the trends presented above, the first of which is that there is virtually no difference in the measured magnetic field when the plasma is flowing when compared the applied magnetic field; the largest difference is 0.2 G. The second notable item is there appears to be no additional acceleration or drag forces present as the parallel ion velocity is essentially flat indicating that the adiabatic conversion from perpendicular to parallel motion is complete. A final observation is that there are two regions of expansion during both time windows for the ion, momentum, and magnetic fluxes: 1) a fast expanding region over the first $\Delta Z \sim 0.6$ m, and 2) a more gradual expansion region over the final $\Delta Z \sim 2$ m. It is useful to compare the rates of expansion for each of the fluxes. Exponential fits were initially used but it was later determined that a power law scaling yielded superior coefficients of determination (> 0.995). The best power law fits are displayed in table 1. These fits show, when comparing the falloff in concentration, that the plasma is not expanding with the magnetic field. Fits to the ion flux data show signs of divergent detachment (expanding ‘faster’ than the magnetic field) during the low energy helicon operation and convergent detachment during ICH when the ion energy increases by a factor of 4. Power law fits to the momentum flux data from the PMFS, which is sensitive to both ions and neutrals, shows only convergent detachment when compared to the magnetic field during both modes of operation. The disagreement between the ion flux and momentum flux data during the helicon phase may be indicative of radial ambipolar forces causing the ions to expand faster than the magnetic field which are overcome when the ion energy

Table 1. Power law scaling (Z^n) fits to the expanding ion, momentum, and magnetic fluxes during both time windows and expansion regions.

Parameter	n, Region 1 ($Z \approx 2.8 - 3.4$ m)		n, Region 2 ($Z \approx 3.4 - 5.4$ m)	
	Helicon	Helicon + ICH	Helicon	Helicon + ICH
Ion Flux	-10.1	-7.8	-5.5	-4.9
Momentum Flux	-7.7	-7.7	-5.0	-4.4
Magnetic Flux	-8.6	-8.6	-5.4	-5.4

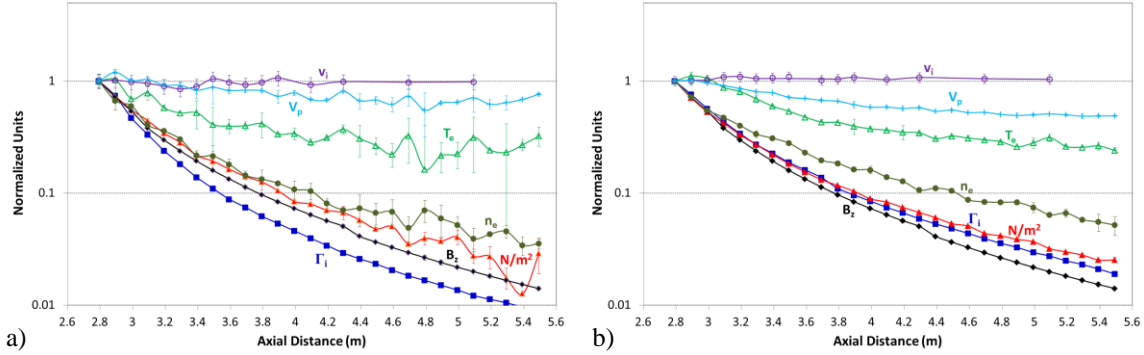


Figure 7. Axial data comparison for multiple plume parameters during both a) helicon and b) helicon + ich modes of operation. Data values are normalized to the closest measured datum point for each parameter.

is increased. Side-by-side comparisons of these data also including electron density/temperature, and plasma potential (from guard-ring probe data) are displayed in Fig. 7. Values are normalized to the most upstream datum point for each parameter. The same trends from the power law fits can be seen in Fig. 7 where neither the ion flux nor the momentum flux data are observed to follow the magnetic flux which is an indication for detached ion flow.

A. Ion Detachment

1. Indications from Mapped Ion Flux and RPA Pitch Angle Scans

The approach of comparing the axial expansions of flux may be expanded to the rest of the plume as a means of verifying detachment. This new method has been developed to compare spatially integrated ion flux and magnetic flux from mapped data throughout the magnetic nozzle region of the exhaust plume and is illustrated in Fig. 8.³⁵ The

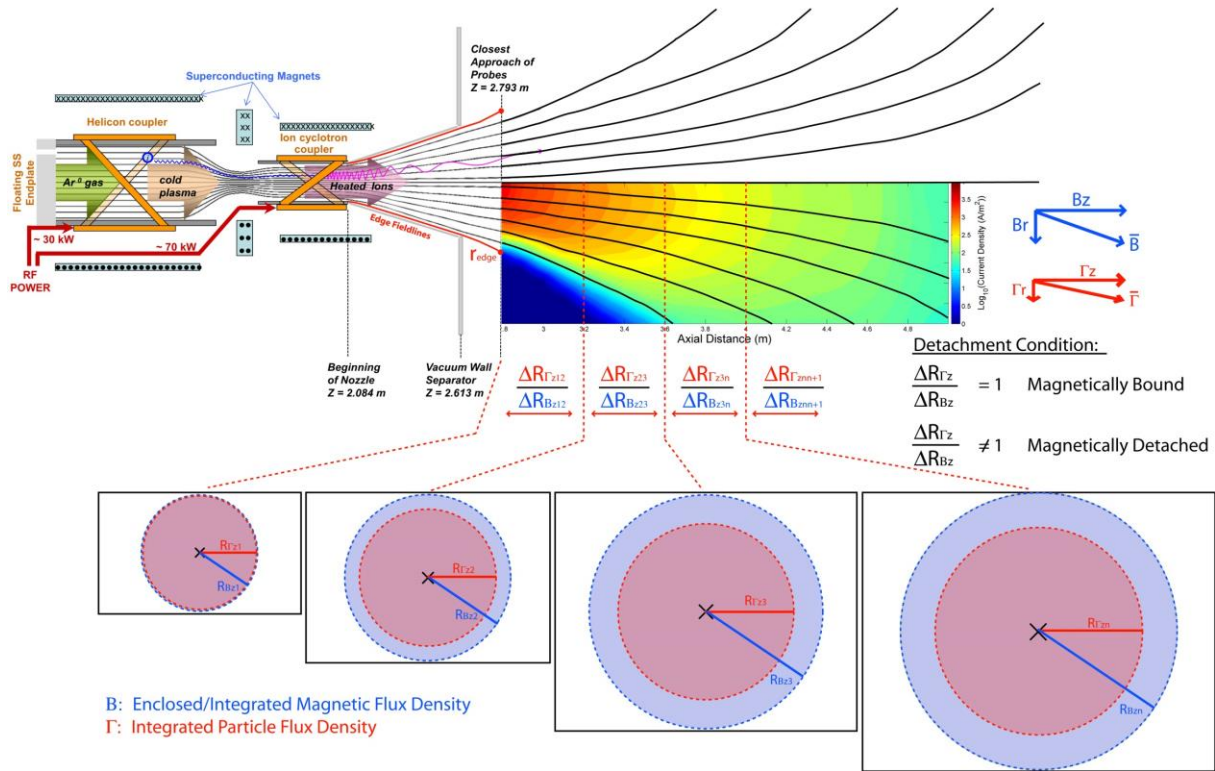


Figure 8. Illustrating the method of spatially tracking lines of constant integrated ion flux and magnetic flux. Convergent detachment is shown (x-section insets) and appears as ion flux (pink) expanding slower than magnetic flux (blue).

focus is turned to ion flux (rather than momentum flux) in order to better understand the behavior of ions in the magnetic nozzle. By comparing the change in radial position of expanded ion and magnetic flux, a detachment condition may be formed which states that if the ratio of these quantities is unity the flow must be considered attached to the applied field. Deviation from unity is indicative of either convergent or divergent detachment. The process begins with the continuity equation under the assumption that charge sources and losses are negligible and that the flow is in steady state:

$$\frac{\partial \rho}{\partial t} + \nabla \cdot (\rho \bar{u}) = S - L \approx 0 \quad (1)$$

This form of the continuity equation is valid based on the steady mass flow rate shown in Fig 5 and losses being minimized due to lower background pressures and interaction cross-sections. The sources term is also presumed negligible based on verification from spectral data of a singly ionized plume, low ion collision rate, and lack of additional external energy sources. The continuity equation permits the measurement of the plasma/magnetic flux expansion without worry of external influences. The ion flux probes are planar probes and restrict the comparison to only the axial components of ion and magnetic flux. The method continues by establishing a baseline integrated ion flux using data taken using a radial scan at the axial position closest to the nozzle ($Z \sim 2.79$ m). The ion flux is numerically integrated outward in radius from the peak of the plume to r_{edge} , a position determined from a geometric projection of the magnetic field from the inner wall of the engine core. The equations pertinent to this numerical integration, assuming azimuthal symmetry, are:

$$\Gamma_{iz}(r) = 2\pi \int_0^r \frac{J_{iz}}{q} r dr \quad (2)$$

$$f_i(r) = \frac{\Gamma_{iz}(r)}{\Gamma_{0z}(r_{edge})} \quad (3)$$

$$\Phi_z(r) = 2\pi \int_0^r B_z r dr \quad (4)$$

$$f_\Phi(r) = \frac{\Phi_z(r)}{\Phi_{0z}(r_{fi})} \quad (5)$$

Equations (2) and (3) describe the radial ion flux integration and ion plume fraction, f_i , which are used to map lines of constant integrated ion flux throughout the extent of the magnetic nozzle. Equations (4) and (5) are similar to the particle flux equations, except they detail the radial integration of magnetic flux and map lines of constant *enclosed* magnetic flux, that is, the expansion of the amount of magnetic flux enclosing the baseline ion flux. This

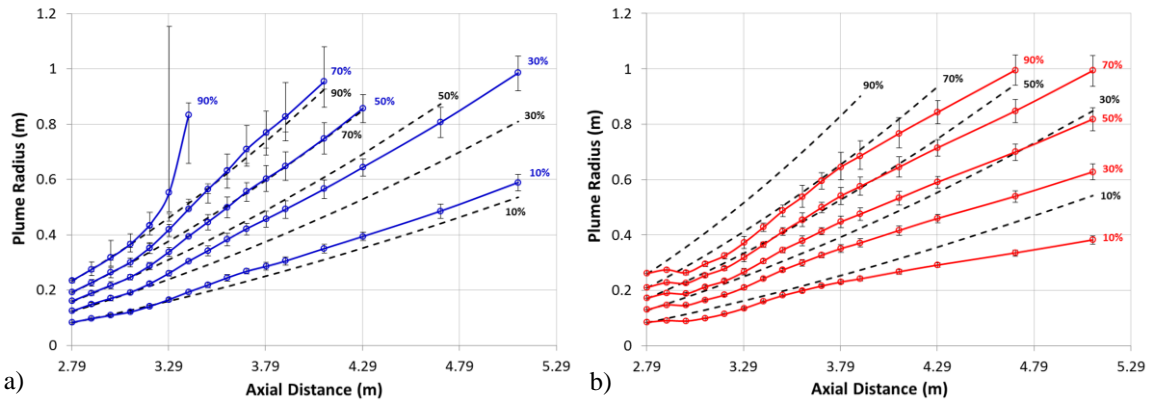


Figure 9. Lines of constant integrated ion flux during the a) helicon and b) helicon + ICH phases of operation compared to lines of constant enclosed magnetic flux (black dashed). To avoid excessive clutter only odd plume fractions (by 10%) are displayed.

set of operations was performed at each axial location where a radial profile data were taken, and the fluxes were integrated outward until the flux matched discrete values of the plume fraction ($f_i, f_\phi = 0.05$ to 0.9 , in steps of 0.05). Results of these integrations are presented in Fig. 9. The data displayed along each of the trends are where the integration was able to measure the value of the ion plume fraction. Some of the plotted series have fewer points as a result of the integration failing to measure certain values of the ion plume fraction within the radial limits of the translation stage. Resultant error bars are displayed, having been computed and passed through the integration, assuming the maximum and minimum error of the baseline profile which propagates systematic uncertainty and errors introduced during interpolation. The large upper error bar during the helicon phase was a result of the numerical integration failing to measure the ion plume fraction and defaulting to the maximum radial position.

There are several notable trends to point out from the plotted integrations. First and foremost is that the ion flux deviates from the magnetic flux that originally encloses the plasma for all plume fractions. The difference between the helicon and helicon + ICH cases has no bearing on *if* the ion flow separates from the applied magnetic field, but more on where the deviation begins. The addition of energy to the ions via ion cyclotron resonance (ICH) causes a doubling of parallel ion velocity ($4 \times E_i$) resulting in the separation from the magnetic field to occur ~ 0.4 m further upstream. The second observation is that these integrations agree with the axial data comparisons in that the helicon case shows divergent detachment, where the helicon + ICH is convergent. The detached ion flow for the helicon case may cross back over the magnetic field lines further outward and/or downstream as the magnetic field turns back on itself, but that is inconclusive due to limitations of translation stage measurement range.

Another aspect of these lines of constant ion flux is the trend of the lines themselves. Focusing on the helicon + ICH case (Fig. 9b), one may divide the flow into separate regions based on the behavior of the flow: A magnetized region, a detached but expanding region, a transition region, and a ballistic/linear expansion region. The ions appear to follow the magnetic field for only a short distance ($\Delta Z \sim 0.1$ m) before deviating from the enclosed magnetic flux from $Z \approx 2.8$ m to 2.9 m. Shortly after separating from the magnetic nozzle field the ions undergo a gradual expansion, radially outward, for approximately $\Delta Z \sim 0.6$ m between $Z \approx 2.9$ m to 3.5 m. Although the ions have detached from the applied magnetic field, they are still subject to inter-particle/wave forces which are believed to influence this radial expansion. A transition region is seen as the trends begin to roll over beginning with the inner plume ($f_i = 10\%$) at $Z \sim 3.5$ m ending along the plume edge ($f_i = 90\%$) at $Z \sim 3.9$ m. Downstream of this transition region ($Z > 3.9$ m) the lines of constant ion flux expands linearly, exhibited by linear fits with excellent coefficients of determination (> 0.999), and the ion plume is therefore ballistic. Throughout these regions the interactions between the ions and magnetized electrons become important and shall be discussed further below.

An alternative method to comparing the expansion rates of ion and magnetic fluxes for confirming detachment one may compare ion velocity vectors to magnetic field vectors through measurement of the pitch angle distribution. The distribution of ion velocity vectors is measured using an articulating RPA repositioned by a step motor driven goniometer to change the angle of the entrance grids with respect to the incoming plasma flow. An angular scan from $\theta = 0^\circ$ to 90° , at intervals of $\Delta\theta = \{5^\circ, 10^\circ, \text{ and } 20^\circ\}$, was performed at five radial locations between $R = 0$ to 0.4 m at an axial position of approximately 2 m downstream of the nozzle throat. An angle of $\theta = 0^\circ$ corresponds to the RPA oriented parallel to the nozzle axis. Contour plots of the ion velocity distribution function from this data as a function of perpendicular versus parallel ion velocity are presented in Fig. 10. The local magnetic field vector is shown in each plot along with the magnitudes of each component as an inset.

Much of the plume behavior exhibited in the previous data can be seen in these pitch angle distributions. For example, during helicon operation the ions were observed to expand ‘faster’ radially than the magnetic field and signatures of this are seen as a broadened angular distribution with increasing radial position. During helicon + ICH operation the ions remain fairly well directed ($\theta < 45^\circ$) regardless of radial position suggesting convergent flow. In either case the ions do not show any signs of predominant magnetization especially at the larger radial distances where the field has begun to curve away. If the ions were magnetized much of the distribution would be expected to be more preferentially organized near the angle of the magnetic field vector. This effect is not observed and the ion flow appears to ignore the influences of the magnetic field. This combined behavior of the ions offers a secondary confirmation that the ions are effectively detached from the magnetic nozzle at this point in the plume.

2. Comparison with Theory

Given the above data presents evidence of ion flux separating from its own magnetic flux surfaces, is this detachment consistent with any of the published theories? One of the leading theories involves MHD field line stretching^{4,5} where the flow of a single fluid becomes energetic enough to drag the magnetic field lines along with the plume negating the necessity for field line separation. This ‘frozen-in flow’ theory is inconsistent with the data as it requires large scale changes to the magnetic field structure in the plume, which was neither observed in the

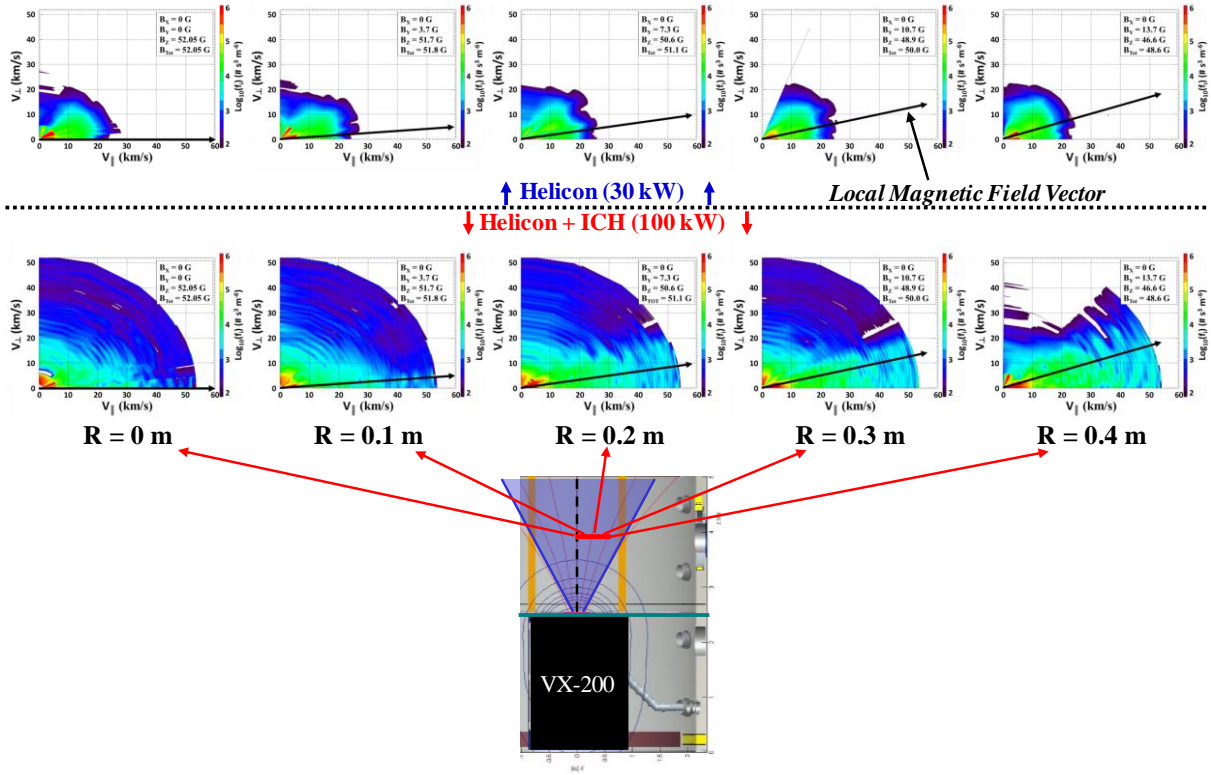


Figure 10. Contour maps of the ion velocity distribution function as a function of V_{\perp} and V_{\parallel} arranged according to radial position (columns), helicon (top row), and helicon + ICH (bottom row) operation. The local magnetic field vector is overlain in each plot (black arrow). A diagram illustrating the relative position of the measurements is provided below the contour maps.

axial data (Fig. 6) nor in an expanded version of this study¹. Another theory, serving as a fundamental lower limit to detachment, known as electron inertia⁸ where ions and electrons are electrostatically bound only drifting across the magnetic field lines if certain conditions are met. A governing parameter in this electron inertia theory is a scaling parameter, G , that involves the cyclotron frequencies as well as the plume radius and velocity at the nozzle throat and it is stated that smaller values of G are more favorable for detachment⁸. The scaling parameter values for this experiment are 4.3×10^6 and 1.1×10^6 for plasma during helicon and helicon + ICH, respectively. Accordingly, less than 1% of the plume should be separating within the premise of this theory, which is not the case (Fig. 9). Electron inertia may find more applicability upon taking into account additional effects found in essentially all plasmas.

The theory most consistent with the ion detachment data presented above is a loss of adiabaticity^{6-7,36}. This theory is essentially one of demagnetization where the ions are unable to change gyro-motion parameters on the same scale as the diverging magnetic field. The diverging nozzle field enables perpendicular to parallel ion velocity vector conversion when the magnetic moment, μ , is conserved. The magnetic moment is conserved so long as the action integral in Faraday's law remains valid and breaks down when the particle gyroorbit becomes too eccentric. An equation illustrating this magnetic moment breakdown is⁶:

$$\frac{\Delta r_{Li}}{r_{Li}} \approx \frac{\Delta \Omega_i}{\Omega_i} = \frac{v_i}{f_{ci}} \frac{|\nabla B|}{B} \quad (6)$$

This states that the magnetic moment will no longer be conserved when the change in Larmor radius becomes comparable to itself, or when the ratio of the Larmor radius to magnetic field scale length ($L_B \sim B/|\nabla B|$) is of order unity. Along the region where the lines of constant ion flux begin to diverge from the magnetic flux in Fig. 9, the right hand side of Eqn. (6) has a range of 1.6 – 4.3 and 2.2 – 4.9 for the helicon and helicon + ICH phases, respectively. These ranges are both of order unity, are consistent in magnitude across each detachment zone, and show agreement between ion flux probe data with magnetometer/RPA data. Ion detachment via loss of adiabaticity is entirely plausible if not considered confirmed altogether.

B. Electron Cross-Field Transport

Up to this point most of the focus has been on the dynamics of the ions in the flow. Electrons, unlike the ions, are presumed to still be magnetized as the right hand side of Eqn. (6) is still a few orders of magnitude below unity (< 0.013) over the entire measurement range of this experiment. Therefore in the scenario that the ions have become demagnetized electrons must find a means of crossing the magnetic field lines, until they also become non-magnetized, otherwise large scale electric fields will arise as space-charge limits become unbalanced. The latter is not occurring given that the plasma potential data from Fig. 7 displays no large transitions indicating only moderate DC electric fields. This conclusion leaves the possibility that magnetized electrons will either cause drag forces to arise on the ions, be impelled to cross the field lines in the wake of the ions, or both to some degree. In the case of electrons crossing the field lines in pursuit of the ions, it must be required that they do so at approximately the same velocity as the ions in order to preserve quasineutrality. It is then necessary to look for signatures of cross-field electron transport across the measurement region.

1. Coulomb Collisions

One of the more straight forward mechanisms for electrons to cross magnetic field lines is through collisions. Estimation of the classical collision frequency was done using the test particle model for electrons and singly charged ions³⁷:

$$\nu_{\alpha\beta}(V) = \frac{n_{\beta} q^4 \ln \Lambda}{2\pi \epsilon_0^2 m_{\alpha}^2 V^3} [\phi(a_{\beta} V) - \psi(a_{\beta} V)] \quad (7)$$

$$a_{\beta} = \sqrt{\frac{m_{\beta}}{2k_B T_{\beta}}} \quad (8)$$

where the subscripts α and β refer to the test particle and field particles, respectively, V is the test particle velocity, $\ln \Lambda$ is the Coulomb logarithm, $\phi(x)$ is the error function, and $\psi(x)$ is the derivative of $\phi(x)$. Equation (7) may be simplified by using limiting or asymptotic values for $\phi(x)$ and $\psi(x)$, a valid assumption in this case, and in the form of Trubnikov³⁸ collision frequencies perpendicular and parallel to the magnetic field may be computed. Estimated collision frequencies and inverse Hall parameters (ν_c / Ω_e) taken along the nozzle axis are shown in Fig. 11. Collisions with neutrals are shown for reference and were computed using the NRL formulary³⁷. The test particles are depicted

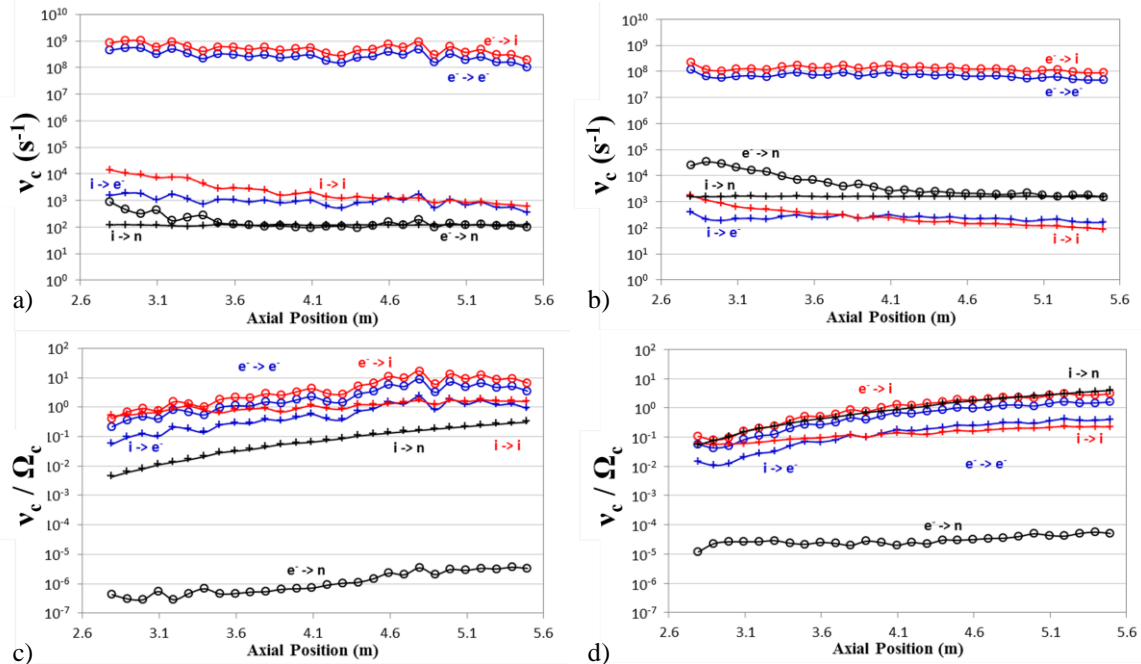


Figure 11. Collision frequency and inverse Hall parameter data along the nozzle axis during helicon (a,c) and helicon + ICH (b,c) operation. Test particles are represented by symbols (o electron, + ion) while line color indicates the scatterer (blue ~ electrons, red ~ ions, and black ~ neutrals).

by symbols (o for electrons, + for ions) and the scattering particles are indicated by line color (blue for electrons, red for ions, and black for neutrals).

These data show that there are large differences in terms of collision frequency between the electrons and ions. Collisions from the ions as well as collisions upon neutrals can essentially be ignored. The electron collision frequency and its role in diffusion must be considered in the transport analysis. The inverse Hall parameter, which is a measure of the number of collisions per gyro-orbit, data shows that despite being able to complete several gyrations about the magnetic field lines before a collision occurs that net transport of the electrons is possible.

2. Cross-Field Diffusion

The collision estimates above show that while electron collisions may not be ignored, the question is then whether the rate of cross-field transport is sufficient to match the outflow rate of the ions ($\sim 13\text{-}17$ km/s during helicon and $\sim 27\text{-}31$ km/s with the addition of ICH). Net cross-field transport requires that the colliding particle undergoes a $\pi/2$ deflection. Since electron \rightarrow electron collisions, despite having a collision frequency near electron \rightarrow ion collisions, have an equal probability of inward versus outward deflection and cannot account for net transport. It is common practice to therefore ignore electron \rightarrow electron collisions as a net transport mechanism. Electron \rightarrow ion collisions, due to the mass difference, deflect the electrons while the ions are relatively unaffected and can thus lead to net electron transport. In order to estimate the cross-field velocity due to electron \rightarrow ion collisions, the equations governing this process, derived from Fick's Law, are³⁹⁻⁴¹:

$$u_{\perp} = \pm \mu_{\perp} E_{\perp} - D_{\perp} \frac{\nabla n_{\perp}}{n} + \frac{u_E + u_D}{1 + \left(\frac{v_{ei}}{\Omega_e}\right)^2} \quad (9)$$

$$D_{\perp} = \frac{k_B T_e}{m_e v_{ei}} \frac{1}{1 + \left(\frac{\Omega_e}{v_{ei}}\right)^2} \quad (10)$$

Equation (9) is a generalized cross-field electron velocity that contains contributions from particle mobility ($\mu_{\perp} = qD_{\perp}/k_B T_e$) reacting to an electric field, diffusion across a density gradient (Eqn. 10), and components of the $E \times B$ and diamagnetic drifts (u_E and u_D). The DC electric field is taken from the negative gradient of the plasma potential using data from the guard-ring Langmuir probe and the component perpendicular to the magnetic field is computed using the angle between the electric field and magnetic field vectors. The diffusion coefficient (including collision parameters) and density gradient are computed using data taken from the guard-ring probe, RPA, and magnetometer. The $E \times B$ and diamagnetic drifts are by definition perpendicular to the gradients in potential and density, which is along the azimuthal component of this system and do not contribute to the net axial/radial transport and are not used here but are treated with other drift motion in more detail in a separate work¹.

The perpendicular cross-field velocity of electrons due to electron \rightarrow ion collisions has been computed using mapped quantities and is presented in Fig. 12. Although the figures appear noisy, common as taking gradients accentuates noise in data, valuable trends still emerge. The largest cross-field velocities are seen along the plume edges (outside the black lines) where the density gradient is large and the diffusion contribution dominates. Inside of the plume the mobility contribution is greater due to DC electric fields within the plasma. None-the-less, electron \rightarrow ion collisions cannot alone account for the velocities needed to match the ions as they are insufficient by

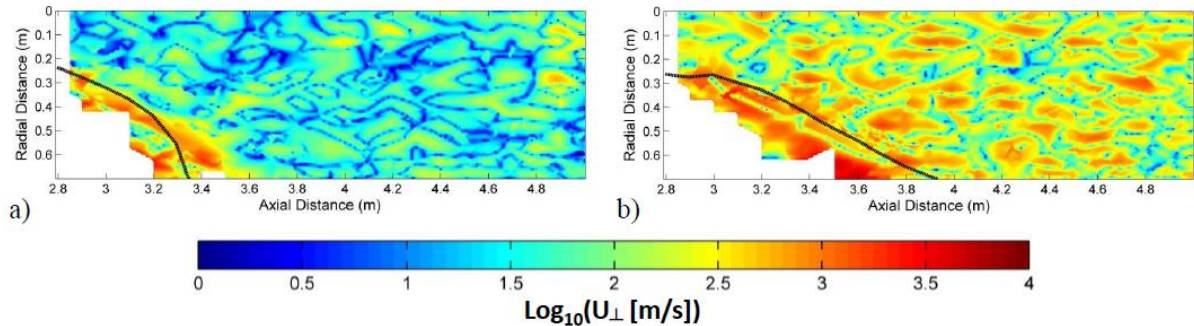


Figure 12. Net cross-field diffusion due to electron \rightarrow ion collisions during a) helicon and b) helicon + ICH operation. An effective plume edge (black), taken from the ion flux line $f_i = 0.9$, is overlain for reference.

at least an order of magnitude. Additional processes must be occurring to facilitate the detachment process.

3. Anomalous Transport

Anomalous resistivity has been mentioned as a possible mechanism to enhance cross-field particle transport in the detachment process^{8-9,18,42}. It is described as a means to increase the effective collision rate above inter-particle collisions, up to the Bohm limit ($D_{\text{Bohm}} = T/B$), through interactions between particles and a high frequency wave (e.g. oscillating electric field). The waves are introduced through turbulence as the plasma responds to perturbing instabilities. The modified two-stream instability (MTSI) has been mentioned as viable candidate³³ in curved magnetic fields as the ions and magnetized electrons drift apart, with particular interest in frequencies near the lower hybrid where both particles responses are maximized (i.e. lower hybrid drift instability, LHDI). As a result of these instabilities it has been found that the fluctuations in density and electric field are in phase⁴² and creates an effective resistivity above the collisional value³³:

$$\eta_{\text{eff}} = \eta_c + \eta_{\text{AN}} \approx \eta_c + \frac{\langle \tilde{n}_e \tilde{E} \rangle}{qu_{\text{de}} \langle \tilde{n}_e \rangle^2} \quad (11)$$

where the tilde denotes fluctuating quantities, $\langle \rangle$ represents the time average of enclosed parameters, and u_{de} is drift velocity of the electron beam relative to the ion beam. The contribution from anomalous resistivity (η_{AN}) would normally include oscillating magnetic field components⁴³, but are presumed negligible compared to the electric field. It is left as future work to measure the high frequency components of the magnetic field and its role in anomalous transport. The effective resistivity modifies the perpendicular diffusion coefficient (and likewise electron mobility) to⁴⁴:

$$D_{\perp} = \frac{k_B T_e}{qB} \left(\frac{\Omega_e \tau_{\text{eff}}}{1 + (\Omega_e \tau_{\text{eff}})^2} \right) \quad (12)$$

$$\tau_{\text{eff}} = \frac{m_e}{\eta_{\text{eff}} q^2 n_e} \quad (13)$$

The effective momentum transfer time, τ_{eff} , is the time interval for momentum exchanges between the electrons and fluctuating electric field and is the inverse of the effective collision frequency.

If anomalous transport were to be applicable in this setup, signatures of a high frequency electric field, particularly near the lower hybrid frequency, should arise throughout the regions of the nozzle where ions have deviated from the magnetic field. The high frequency electric field probe was used to explore these effects. Due to the orientation of the probes' electrodes, only the radial component of the electric field (E_r) was measured searching frequencies up to 10 MHz. Recalling that the probe was located ~ 33 cm downstream the other diagnostics, due to material thermal limitations, the regions indicating ion separation were unable to be measured. Nevertheless studying high frequency phenomena in the expanding, transition, and ballistic regions as parsed by the ion flux data is valuable. Spectra have been taken and mapped out as a function of radial position at discreet axial locations for both phases of VX-200 operation and are presented in Fig. 13. Each contour plot is comprised of the logarithmic value of the radial electric field as a function of frequency and radius and arranged by increasing Z position from bottom to top. A thin black line marks the lower hybrid frequency (f_{LH}) as a function of radial position.

There appears to be an overall trend of increasing radial electric field strength at higher frequencies, both in and out of the plasma flow. It is yet to be determined if this effect is dependent upon the probe/electronics or perhaps a result of the chamber/tuning cavity environment. Unique to the case of hotter ions (during helicon + ICH) is a distinct structure or grouping of electric field peaks that forms near the edge of the flow coincident with regions of lower magnetic field radial curvature. This observation is significant since the lower curvature may provide a greater divergence of the electrons from the detached ions allowing the instability to form. The greatest amplitude E_r along the edge of the flow was 740 V/m at a frequency of 5.51 MHz which is approximately $\sim 3f_{\text{LH}}$ suggesting the LHDI may be involved. This edge structure spreads out and dissipates with increasing axial distance before disappearing altogether beyond $Z > 3.93$ m. The locations where this E_r structure spreads to the interior of the plume line up well with the ion flux transition region where the flow linearizes between $3.5 \text{ m} < Z < 3.9 \text{ m}$ in Fig. 9. The vanishing of the structure altogether in the weaker magnetic field correlates well with the ion flux ballistic/linear region $Z > 3.9 \text{ m}$ in Fig. 9, indicating the instability is no longer active, electron/ion separation has minimized, and the flow has

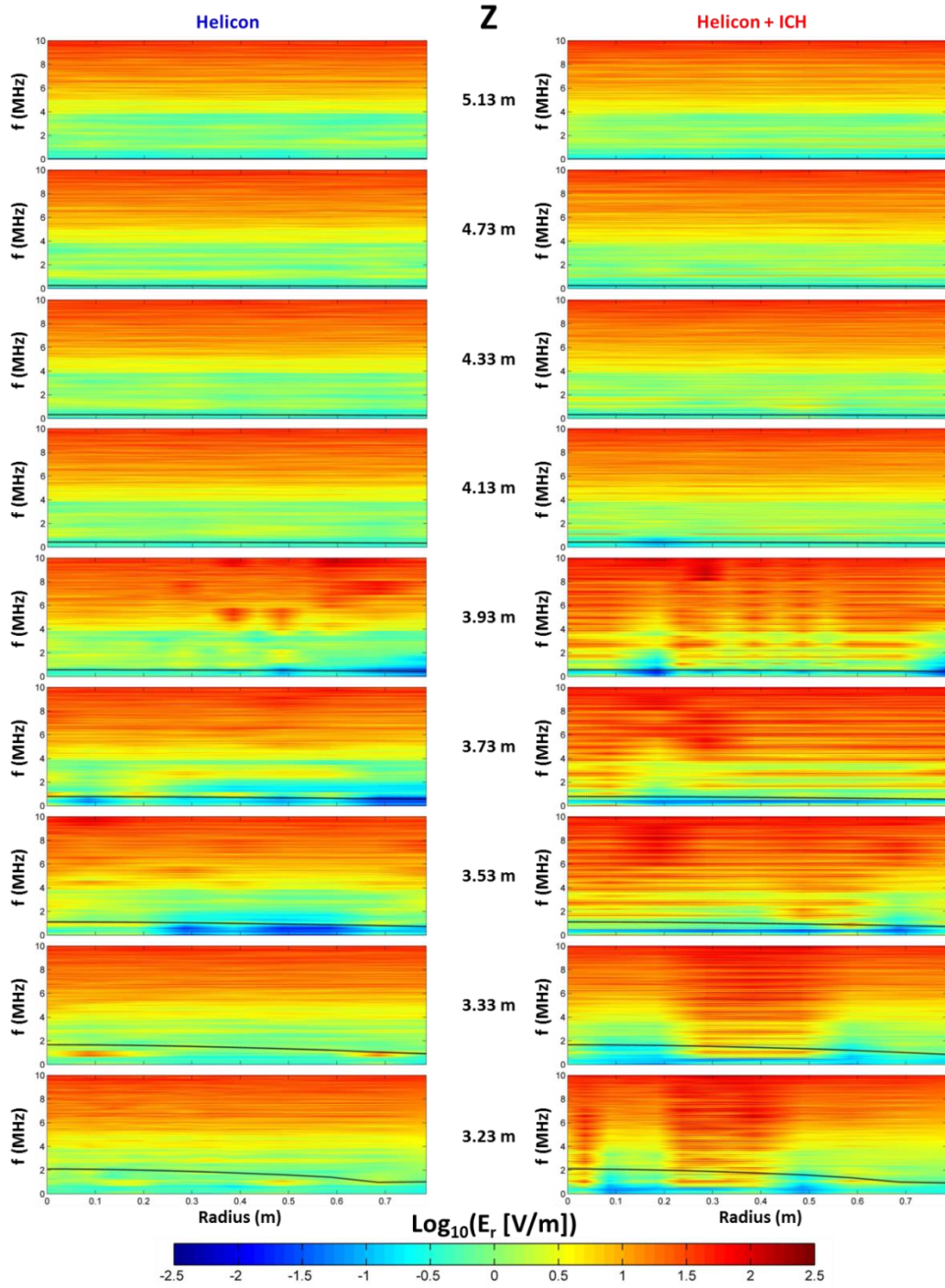


Figure 13. Composition of radial electric field strength contours as a function of frequency and radius for both helicon (*left*) and helicon + ICH (*right*) operation. The contours are arranged by axial location of the scan (*rows, increasing bottom to top*). The lower hybrid frequency as a function of radius is plotted for reference (*black line*).

effectively detached from the magnetic nozzle. The structure is not readily observed during phases of operating the helicon source alone, which either does not exist or was not measured far enough radially. It is left as future work to explore electric and magnetic field phenomena at higher frequencies, at greater radii, and along multiple vector components.

4. Force Balance

It has just been shown that a strong high frequency electric field develops along the edges of the plume. Does this mean that anomalous cross-field transport of electrons is a certainty? Not necessarily, especially in the regions of the nozzle where the magnetic field is prohibitive, but it is one of the possible outcomes. As indicated earlier in this section, the behavior of the flow will ultimately depend upon an electrostatic force balance between the ions and electrons and how each respond to the fluctuating electric fields in the plume. The ion response to these fluctuating fields will be to follow electrons along the magnetic field lines where the electric fields are large enough to balance or exceed the centrifugal force on the ions, thus trapping them in the magnetic field:

$$\langle \tilde{E}_{\perp} \rangle_{IT} = \frac{m_i v_i^2}{q R_c} \quad (14)$$

where the subscript IT indicates ‘ion trapping’ and R_c is the radius of curvature of the interacting magnetic field line. The electron response is to cross the outer magnetic field lines to follow the ballistic ions along more centrally located field lines. The electric field in this scenario is then the ratio of the cross-field electron velocity to the anomalous mobility:

$$\langle \tilde{E}_{\perp} \rangle_{AN} = \frac{u_{\perp}}{\mu_{\perp}} = v_i \sin \theta B \left(\frac{1 + (\Omega_e \tau_{eff})^2}{\Omega_e \tau_{eff}} \right) \quad (15)$$

The cross-field electron velocity required to abate space-charge buildup is the product of the ion velocity and the sine of the separation angle of the ions and magnetic field line.

The balance of forces, an electrostatic tug-of-war, to determine which process dominates between ion trapping and anomalous resistivity depends upon the localized microscale conditions in the plume. The process requiring the lower electric field strength will saturate and never reach the field strength necessary for the other process to operate. It should then be expected that the ion trapping process will dominate in high magnetic field regions, areas where the radius of curvature is large, and/or for lower ion mass and velocity. Conditions for anomalous resistivity to dominate would then be for heavier or faster ions, lower magnetic fields, larger effective collision frequency, and/or lower radius of curvature.

Based on the measured data and an assumed range of $1 < \Omega_e \tau_{eff} < 16$ (theoretical minimum to experimental equivalent Bohm diffusion)⁴⁴, conditions are permissible for both of these processes to exist in different regions of the plume^[1]. The electric fields required to maintain curvature motion and trap the ions are lower in more upstream regions ($Z < 3.4$ m). Assuming low divergence angles and greater mobility ($\Omega_e \tau_{eff} < 6$), anomalous transport would be the more effective process for axial ranges $Z > 3.5$ m. The region between $3.4 \text{ m} < Z < 3.5 \text{ m}$ would then be a thin zone transitioning between the two processes and are summarized in Fig. 14. These computed regions are consistent with the trends observed in the integrated ion flux data (Fig. 9b). After deviating from the magnetic field the ions flare out radially between $2.9 \text{ m} < Z < 3.5 \text{ m}$ during helicon + ICH, coincident with the ion trapping region. Inflection points in the lines of constant ion flux mark the zone transitioning to ballistic flow between $3.4 \text{ m} < Z < 3.9 \text{ m}$ and are coincident with the estimated anomalous transport region. Beyond $Z > 4.0$ m the trajectories are linear and the fluctuating electric fields have dissipated

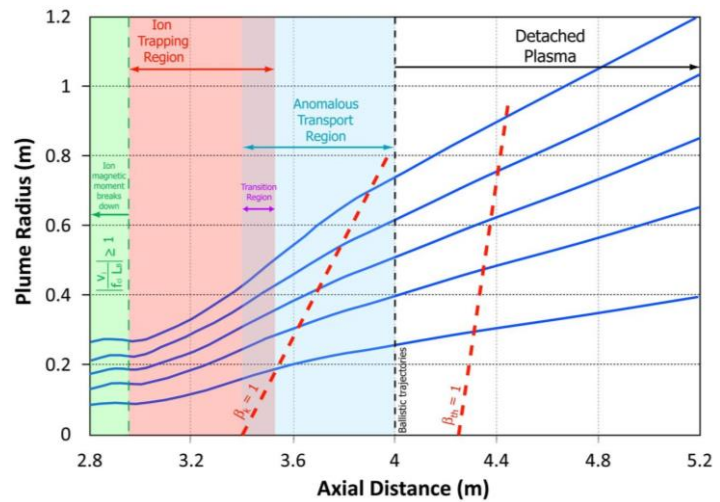


Figure 14. Image summarizing the various regions associated with the detachment process from a magnetic nozzle during helicon + ICH operation. The flow lines (blue) are based on the integrated ion flux and extended out along the linear region. Lines showing the transition above unity for kinetic and thermal ‘beta’ are displayed for reference (red dashed).

indicating that the flow is effectively detached from the magnetic nozzle. The electrons are still magnetized but move with the ions on more centrally located magnetic field lines. They are presumed to eventually become demagnetized in the same manner as the ions, by loss of adiabaticity, in the much weaker magnetic field regions further downstream. Shown for reference are lines of demarcation for the super-Alfvénic flow transition ($\beta_k = 1$) and thermal ‘beta’ ($\beta_{th} = 1$) transition. Curious is that the super-Alfvénic transition covers the span of the anomalous transport region without any significant changes to the magnetic field structure of the applied field as anticipated by MHD detachment theories^{4,5}. The plasma flow is energetically capable of stretching the magnetic field lines, if considered as a single fluid, but if taken as two fluids or even as individual particles the ions could then be considered energetically capable of pulling electrons across the field.

The magnitude of the fluctuating electric field in both the ion trapping and anomalous transport region is sufficient to carry out each process for several of the frequencies where spectral peaks are located. These field strengths can be used to estimate an approximate anomalous transport rate necessary to carry out these observations. Using electric field (at 5.51 MHz), magnetic field, and ion velocity data along the anomalous transport region (3.5 m < Z < 4.0 m) at a divergence angle of 10°, the transport parameter is approximately $\Omega_e \tau_{eff} \sim 4.0$. This value is closer to the ‘Super-Bohm’ values ($\Omega_e \tau_{eff} \sim 2.7$) reported by Brenning et al.⁴⁴ than it is for the commonly accepted, experiment dependent, Bohm value of 16. This estimated transport parameter equates to an effective momentum transfer rate of $\sim 3.5 \times 10^8 \text{ s}^{-1}$ which is a factor of 4±1 above the electron→ion collision frequency. This higher effective collision frequency, in addition to the effects of the oscillating electric field on the classical mobility, would bring the electron cross-field velocity within a factor of two for the required values to match the detached ion velocity¹.

These processes and rates are reported for the more energetic plasma flows during helicon + ICH operation. It appears that ion trapping or radial ambipolar forces dominate the plume behavior for lower ion velocity flow during helicon only operation. Although not directly observed, anomalous transport may still be occurring in the weak magnetic field regions beyond the limits of the translation stage. It may be the focus of future experiments to explore the plume further out in radius during plasma operation at lower ion energy.

IV. Conclusion

An experiment using the VASIMR[®] VX-200 device operating at a power level of 100 kW was carried out in order to map the behavior of plasma flowing through a magnetic nozzle and to study the detachment process. The plasma was not following the applied magnetic field, indicated by data from multiple plasma diagnostics. Key indications of detached flow were from mapped lines of constant integrated ion flux, an RPA pitch angle distribution, and a spatially dependent high frequency electric field. Plasma detachment is best described as a two part process first involving the separation of the ion from the magnetic field through the breakdown of the ion magnetic moment. The second part involves turbulence, created by instabilities, where a fluctuating electric field facilitates competing interactions between detached ions and magnetized electrons. In stronger magnetic field regions the electrons are more tightly bound to the field and the ions are temporarily ‘trapped’ flaring outward as the field expands. As the magnetic field weakens the ions begin to dominate and the electrons respond to the turbulent electric field through enhanced anomalous transport. The electrons cross the magnetic field lines pursuing the ions until the turbulent electric field dissipates and the ion trajectories linearize resulting in an effectively detached plume approximately 2 m downstream of the nozzle throat.

Future work may include making the same measurements out to greater radii, including new hardware to measure the axial component of the high frequency electric field, and explore for effects from a plausible high frequency magnetic field to better characterize anomalous transport rates in the plume. Also possible may be to explore the detachment processes at various VASIMR[®] power levels (i.e. multiple ion energies), propellant flow rates, and propellant species.

References

¹Olsen, C.S., *Experimental Characterization of Plasma Detachment from Magnetic Nozzles*, in *Department of Physics & Astronomy*. Ph.D Dissertation, May 2013, Rice University: Houston. p. 298.

²E. Ahedo, *Plasmas for space propulsion*. Plasma Physics and Controlled Fusion, 2011. **53**(12): p. 124037.

³R. A. Gerwin, et al., *Characterization of Plasma Flow through Magnetic Nozzles*. 1990, Los Alamos National Laboratory. p. 173.

- ⁴A. V. Arefiev and B.N. Breizman, *Magnetohydrodynamic scenario of plasma detachment in a magnetic nozzle*. Physics of Plasmas, 2005. **12**(4): p. 043504-10.
- ⁵B. N. Breizman, M. R. Tushentsov, and A.V. Arefiev, *Magnetic nozzle and plasma detachment model for a steady-state flow*. Physics of Plasmas, 2008. **15**(5): p. 057103-10.
- ⁶M. D. Carter, et al. *Radio Frequency Plasma Applications for Space Propulsion*. in *International Conference on Electromagnetics in Advanced Applications*. 1999. Torino, Italy.
- ⁷K. Terasaka, et al., *Experimental studies on ion acceleration and stream line detachment in a diverging magnetic field*. Physics of Plasmas, 2010. **17**(7): p. 072106-6.
- ⁸E. B. Hooper, *Plasma detachment from a magnetic nozzle*. Journal of Propulsion and Power, 1993. **9**(5): p. 757-763.
- ⁹E. Ahedo and M. Merino, *On plasma detachment in propulsive magnetic nozzles*. Physics of Plasmas, 2011. **18**(5): p. 053504-8.
- ¹⁰E. A. Bering, et al. *High Power Electric Propulsion Using VASIMR(TM): Results from Flight Prototypes*. in *47th AIAA Aerospace Sciences Meeting and Exhibit*. 2009. Orlando, Florida: AIAA.
- ¹¹B. W. Longmier, J.P.S., C. S. Olsen, L. D. Cassady, M. G. Ballenger, M. D. Carter, A. V. Ilin, T. W. Glover, G. E. McCaskill, F. R. Chang Diaz, and E. A. Bering III, *Improved Efficiency and Throttling Range of the VX-200 Magnetoplasma Thruster*. Journal of Propulsion and Power, 2013.
- ¹²F. F. Chen and R.W. Boswell, *Helicons-the past decade*. Plasma Science, IEEE Transactions on, 1997. **25**(6): p. 1245-1257.
- ¹³R. W. Boswell and F.F. Chen, *Helicons-the early years*. Plasma Science, IEEE Transactions on, 1997. **25**(6): p. 1229-1244.
- ¹⁴J. P. Squire, et al. *VASIMR Performance Measurements at Powers Exceeding 50 kW and Lunar Robotic Mission Applications*. in *International Interdisciplinary Symposium on Gaseous and Liquid Plasmas*. 2008. Sendai, Japan.
- ¹⁵L. D. Cassady, et al. *VASIMR(R) Technological Advances and First Stage Performance Results*. in *45th AIAA/ASME/SAE/ASEE Joint Propulsion Conference and Exhibit*. 2009. Denver, Colorado: AIAA.
- ¹⁶B. W. Longmier, J.P.S., L. D. Cassady, M. G. Ballenger, M. D. Carter, C. S. Olsen, A. V. Ilin, T. W. Glover, G. E. McCaskill, F. R. Chang Diaz, E. A. Bering III, and J. Del Valle. *VASIMR(R) VX-200 Performance Measurements and Helicon Throttle Tables Using Argon and Krypton*. in *32nd International Electric Propulsion Conference*. 2011. Wiesbaden, Germany: IEPC.
- ¹⁷B. W. Longmier, et al. *VASIMR(R) VX-200 Improved Throttling Range*. in *48th AIAA/ASME/SAE/ASEE Joint Propulsion Conference*. 2012. Atlanta, Georgia: AIAA.
- ¹⁸A. V. Arefiev and B.N. Breizman, *Theoretical components of the VASIMR plasma propulsion concept*. Physics of Plasmas, 2004. **11**(5): p. 2942-2949.
- ¹⁹E. A. Bering, et al., *Observations of single-pass ion cyclotron heating in a trans-sonic flowing plasma*. Physics of Plasmas, 2010. **17**(4): p. 043509-19.
- ²⁰T. H. Stix, *Ion cyclotron heating of a plasma*. Journal of Nuclear Energy. Part C, Plasma Physics, Accelerators, Thermonuclear Research, 1961. **2**(1): p. 84.
- ²¹J. P. Squire, et al. *Superconducting 200 kW VASIMR(R) Experiment and Integrated Testing*. in *31st International Electric Propulsion Conference*. 2009. Ann Arbor, Michigan: IEPC.
- ²²W. Lochte-Holtgreven, *Plasma Diagnostics*. 2nd ed. American Vacuum Society Classics, ed. A. Press. 1995, New York: AIP Press. 928.
- ²³B. W. Longmier, et al., *Ambipolar ion acceleration in an expanding magnetic nozzle*. Plasma Sources Science and Technology, 2011. **20**(1): p. 015007.
- ²⁴C. S. Olsen, *Ion Flux Maps and Helicon Source Efficiency in the VASIMR VX-100 Experiment Using a Moving Langmuir Probe Array*, in *Physics and Astronomy*. Master's Thesis, May 2009, Rice University: Houston. p. 155.

- ²⁵D. G. Chavers and F.R. Chang-Diaz, *Momentum flux measuring instrument for neutral and charged particle flows*. Review of Scientific Instruments, 2002. **73**(10): p. 3500-3507.
- ²⁶X. Chen, *The impact force acting on a flat plate exposed normally to a rarefied plasma plume issuing from an annular or circular nozzle*. Journal of Physics D: Applied Physics, 2010. **43**(31): p. 315205.
- ²⁷D. G. Chavers, et al. *Momentum and Heat Flux Measurements in the Exhaust of VASIMR Using Helium Propellant*. in *28th International Electric Propulsion Conference*. 2003. Toulouse, France: IEPC.
- ²⁸B. W. Longmier, et al., *Validating a Plasma Momentum Flux Sensor to an Inverted Pendulum Thrust Stand*. Journal of Propulsion and Power, 2009. **25**(3): p. 7.
- ²⁹L. W. Parker and E.C. Whipple, *Theory of a satellite electrostatic probe*. Annals of Physics, 1967. **44**(1): p. 126-161.
- ³⁰E. A. Bering, K. G. Weber, and U.V. Fahleson, *An upper limit on the aperture separation of ion drift meters*, in *Astrophysics and Space Science*. 1982, Springer Netherlands. p. 37-49.
- ³¹Bering III, E.A., F. Chang-Diaz, and J. Squire, *The use of RF waves in space propulsion systems*. 2004.
- ³²T. Hurtig and J. Wistedt, *Probes for high-frequency measurements in a plasma gun*. Review of Scientific Instruments, 2003. **74**(2): p. 1153-1155.
- ³³T. Hurtig, N. Brenning, and M.A. Raadu, *The role of high frequency oscillations in the penetration of plasma clouds across magnetic boundaries*. Physics of Plasmas, 2005. **12**(1): p. 012308-13.
- ³⁴J. S. Bendat and A.G. Piersol, *Random Data Analysis and Measurement Procedures*. Measurement Science and Technology, 2000. **11**(12): p. 1825.
- ³⁵J. P. Squire, et al. *VASIMR(R) VX-200 Operation at 200 kW and Plume Measurements: Future Plasma and an ISS EP Test Platform*. in *32nd International Electric Propulsion Conference*. 2011. Wiesbaden, Germany: IEPC.
- ³⁶K. Terasaka, et al., *Observation of Ion Streamline Detachment and Onset of Azimuthal Rotation in a Diverging Magnetic Field*. IEEE Transactions on Plasma Science, 2011. **39**(11): p. 2470-2471.
- ³⁷J. D. Huba, *NRL Plasma Formulary*, ed. N.R. Laboratory. 2012, Washington DC: The Office of Naval Research.
- ³⁸B. A. Trubnikov, *Particle Interactions in a Fully Ionized Plasma*. Reviews of Plasma Physics. Vol. 1. 1965, New York: Consultants Bureau. 105.
- ³⁹M. A. Lieberman and A.J. Lichtenberg, *Principles of Plasma Discharges and Materials Processing*. 2nd ed, ed. I. John C. Wiley and Sons. 2005, Hoboken: John C. Wiley and Sons, Inc. 757.
- ⁴⁰F. F. Chen, *Introduction to Plasma Physics and Controlled Fusion*. 2nd ed. Vol. 1: Plasma Physics. 1984, New York: Plenum Press. 421.
- ⁴¹D. M. Goebel and I. Katz, *Basic Plasma Physics*, in *Fundamentals of Electric Propulsion*. 2008, John Wiley & Sons, Inc. p. 37-90.
- ⁴²N. Brenning, T. Hurtig, and M.A. Raadu, *Conditions for plasmoid penetration across abrupt magnetic barriers*. Physics of Plasmas, 2005. **12**(1): p. 012309-10.
- ⁴³E. Y. Choueiri, *Anomalous resistivity and heating in current-driven plasma thrusters*. Physics of Plasmas, 1999. **6**(5): p. 2290-2306.
- ⁴⁴N. Brenning, et al., *Faster-than-Bohm Cross-B Electron Transport in Strongly Pulsed Plasmas*. Physical Review Letters, 2009. **103**(22): p. 225003.